# High Precision Raman Distributed Fiber Sensing Using Residual Composite Dual-Convolutional Neural Network

Haosen Guo , Jian Li , Member, IEEE, Xiaohui Xue , and Mingjiang Zhang , Member, IEEE

Abstract-Raman distributed optical fiber sensing has the unique ability to measure the spatially distributed profile of temperature that are of great interest to numerous field applications. However, the sensing performance is severely limited by the signal-to-noise ratio (SNR). The existing SNR enhancement schemes have drawbacks such as increased system complexity, degradation of sensor performance metrics such as spatial resolution, poor denoising performance, etc. Here, we report the Raman residual composite dual-convolutional neural network (RRCDNet), a novel convolutional neural network-based denoising model for one-dimensional signals specifically tailored to Raman distributed fiber sensing. The RRCDNet-enhanced Raman distributed fiber sensor system dramatically improves the temperature precision by more than a factor of 100, from 7.57 °C to 0.06 °C, without hardware modification or degradation of other performance metrics. At the same time, RRCDNet can also enhance other optical fiber sensor systems with one-dimensional signals, such as Rayleigh and Brillouin sensing systems.

*Index Terms*—Neural networks, optical fiber sensors, raman scattering, signal denoising.

### I. INTRODUCTION

ISTRIBUTED optical fiber sensors [1], [2] provide a method for measuring the spatially distributed profile of environmental quantities, such as temperature [3], vibration [4], [5], strain [6], [7], electromagnetic fields [8], and gas sensing [9], by analyzing specific optical effects activated along optical fibers. And Raman distributed optical fiber sensing system

Manuscript received 22 August 2023; revised 15 November 2023; accepted 12 February 2024. Date of publication 15 February 2024; date of current version 16 May 2024. This work was supported in part by the National Natural Science Foundation of China (NSFC) under Grant 62205234, Grant 62075151, Grant 62105234, in part by the Fundamental Research Program of Shanxi Province under Grant 202103021223042, in part by the Scientific and Technological Innovation Programs of Higher Education Institutions in Shanxi, and in part by the Shanxi-Zheda Institute of Advanced Materials and Chemical Engineering. (Corresponding authors: Jian Li; Mingjiang Zhang.)

Haosen Guo, Jian Li, and Xiaohui Xue are with the Key Laboratory of Advanced Transducers and Intelligent Control System, Ministry of Education, Taiyuan University of Technology, Taiyuan 030024, China (e-mail: 799435433@qq.com; lijian02@tyut.edu.cn; xuexiaohui@tyut.edu.cn).

Mingjiang Zhang is with the College of Physics, Taiyuan University of Technology, Taiyuan 030024, China, and also with the Shanxi-Zheda Institute of Advanced Materials and Chemical Engineering, Taiyuan 030032, China (e-mail: zhangmingjiang@tyut.edu.cn).

Color versions of one or more figures in this article are available at https://doi.org/10.1109/JLT.2024.3366294.

Digital Object Identifier 10.1109/JLT.2024.3366294

[10] analyzes the intensity of temperature-sensitive spontaneous Raman scattering (SpRS) [11] generated by light pulses that are injected into the sensing fiber in order to measure the distribution of the temperature along the sensing fiber [12]. Compared to other distributed optical fiber sensing systems, it has the rapid measurement rate and the straightforward design [13]. The use of Raman distributed optical fiber sensing in pipeline leakage detection [14], power cable monitoring [15], [16], fire alarm systems [17], and other distributed temperature monitoring fields [18], [19], [20] is gaining widespread attention. The performance metrics for the Raman distributed fiber sensing system mainly include temperature measurement accuracy and precision [21], sensing distance [22], and spatial resolution [23]. The signal-to-noise ratio (SNR) has a significant impact on the temperature accuracy and precision of the Raman system. But the Raman system's SpRS signal is about 60–70 dB weaker than the incident pulse power [24] and is also attacked by noise from other devices. This makes the typical Raman distributed fiber sensing signal have a low SNR, which can degrade the temperature accuracy and precision. Therefore, effective techniques need to be investigated to improve the SNR of Raman systems by increasing the intensity of the effective signal or suppressing the noise.

Noise in Raman distributed fiber sensing systems comprises optical noise caused by the failure of the wavelength division multiplexer (WDM) [25] to cleanly eliminate Rayleigh scattered signals, as well as electrical noise caused by avalanche photodiodes (APD) [26] and other circuit devices. The Rayleigh optical noise is structured and increases the total intensity of the Raman distributed fiber sensing signal, decreasing the temperature curve's accuracy. And the electrical noise is assumed to be unstructured and have a zero mean, decreasing the temperature precision. The Rayleigh optical noise can be suppressed using simple Rayleigh optical noise reduction [27], [28]. And there are two primary ways to suppress electrical noise, the first of which employs pulse coding [29] or special fiber [30], [31] to boost the SpRS signal in the Raman distributed optical fiber sensing systems to lower the relative amplitude of electrical noise [32]. But these methods will increase the system's complexity and expense. The second of which uses denoising algorithms to directly reduce electrical noise in the Raman distributed fiber sensing system, has attracted a great deal of interest from researchers because it does not increase the sensor's hardware cost [1].

Numerous denoising algorithms have been proposed to improve the temperature precision of Raman distributed fiber sensors. These algorithms decompose the data according to a particular criterion and separate the noise from the data. They include the short-time Fourier transform [33], the empirical modal decomposition [34], and the Wavelet denoising [35], [36], [37]. But these denoising algorithms have the problems of requiring manual adjustment of parameters, having poor denoising performance, and deteriorating the spatial resolution, a key system metric that is susceptible to degradation during the denoising process. In order to solve the aforementioned problems, neural network-based denoising algorithms have been proposed [38], [39].

Neural networks [40] perform denoising by learning prior knowledge, which can be obtained by training datasets of noise-to-clean or noise-to-noise [41]. The intensity of the signal point of Raman distributed fiber sensors is usually related to its nearby points. Coincidentally, among the many neural network structures, the structure of the Convolutional Neural Network (CNN) [42] makes it possible to associate each signal point with its neighboring signals via convolution, allowing signal features to be easily extracted and the signal's primary components to be identified for noise removal. In the field of deep learning for denoising Raman distributed fiber sensing signals, the onedimension Denoising Convolutional Neural Networks (1DD-CNN) [43] algorithm has attained successful denoising results. We reproduced 1DDCNN, which is unquestionably superior to wavelet denoising in many metrics. However, 1DDCNN's ability to remove low-frequency noise still needs to be improved. And it is well known that when a signal is denoised, a portion of the effective signal is inevitably lost, and this phenomenon is significantly more severe than with wavelets in 1DDCNN, resulting in a drift of the temperature curve and loss of temperature accuracy.

To solve the shortcomings of wavelet denoising and the 1DD-CNN, Raman's residual composite dual-convolutional neural network (RRCDNet), a novel CNN-based denoising network specifically tailored to Raman distributed fiber sensing signals, is proposed. And the article has the following contributions: First, RRCDNet employs a dual-CNN structure to enhance learning ability and dilated convolution to expand the perceptual field and reduce computing costs. In addition, RRCDNet uses residual learning, batch normalization, and Kaiming initialization techniques to accelerate the network's convergence and improve its denoising performance. Second, the spaced sampling and reconstruction greatly improve the network's ability to suppress low-frequency noise. Third, the paper investigates the noise characteristics of the Raman signal, and its qualitative analysis shows that the noise of the Raman signal approximates additive Gaussian white noise. And an analysis of the amplitude distribution and power spectral density is performed in order to inform the construction of the RRCDNet's training set. Fourth, the SNR of the Raman distributed fiber sensing signal cannot be calculated efficiently because SNR is mostly estimated in practical applications, and RRCDNet itself is a high-performance denoising method [43], [44]. To solve the problem, two metrics, average noise and the structural similarity index measure (SSIM)

[45], were introduced from the perspective of filtered-noise to address the problem. Final, experiments have shown that RRCDNet is one of the best performing denoising methods in Raman distributed fiber sensing scheme to our knowledge. After processing by RRCDNet, the smoothness of the temperature curve of the high-noise signal averaged 5000 times is improved from 1.478 to 0.0051, an improvement of about 300 times. And the temperature precision is greatly improved by a factor of 100 from 7.57 °C to 0.06 °C peak-to-peak (±0.03 °C). To our knowledge there is no Raman distributed optical fiber sensing scheme that achieves such high temperature precision. The trained RRCDNet processes the Raman signal end-to-end in approximately 0.3 seconds without requiring manual parameter or threshold adjustments and without degrading other performance metrics.

#### II. DENOISING ALGORITHMS AND METRICS

For a raw Raman distributed fiber sensing signal y, the signal denoising problem can be represented by y=x+v where x is the ideal Raman distributed fiber sensing signal without any noise, and v is the additive Gaussian white noise, which is unstructured and have a zero mean. The majority of the effective signal energy is localized at lower frequencies, with some dispersion at higher frequencies, and has specific structures. The distribution of noise energy has a similar magnitude at both low and high frequencies, but with a tendency for higher energy levels in the higher-frequency range, and has non-smooth structure. It is impossible to totally eliminate the noise from the signal or have no influence on the effective signal x at all during the denoising process.

## A. Denoising Process

The denoising processes are as follows: First, the signal is preprocessed by spaced sampling, as shown in Fig. 1(b), where the signal sequence is divided into four equal-length subsequences (4-divided sampling), so that the low-frequency noise can be transformed into the higher-frequency noise for the subsequent denoising process. Second, the preceding signal subsequence is fed into RRCDNet for denoising, respectively. Third, the subsequence of the denoised signal is reorganized into the complete denoised signal sequence in the same order as before sampling.

### B. Preprocessing

Conventional denoising techniques have proven effective at suppressing high-frequency noise but have limited ability to suppress low-frequency noise. Alternatively, they can effectively suppress low-frequency noise, but at the cost of significant loss of useful data. In comparison to the conventional technique, RRCDNet has a notable capacity to suppress low-frequency noise while exhibiting little degradation of the effective signal. Drawing upon the benefits of RRCDNet, we used preprocessing (as shown in Fig. 1(b)) with interval sampling. This technique facilitates the conversion of low-frequency components into higher-frequency components, hence augmenting the ability

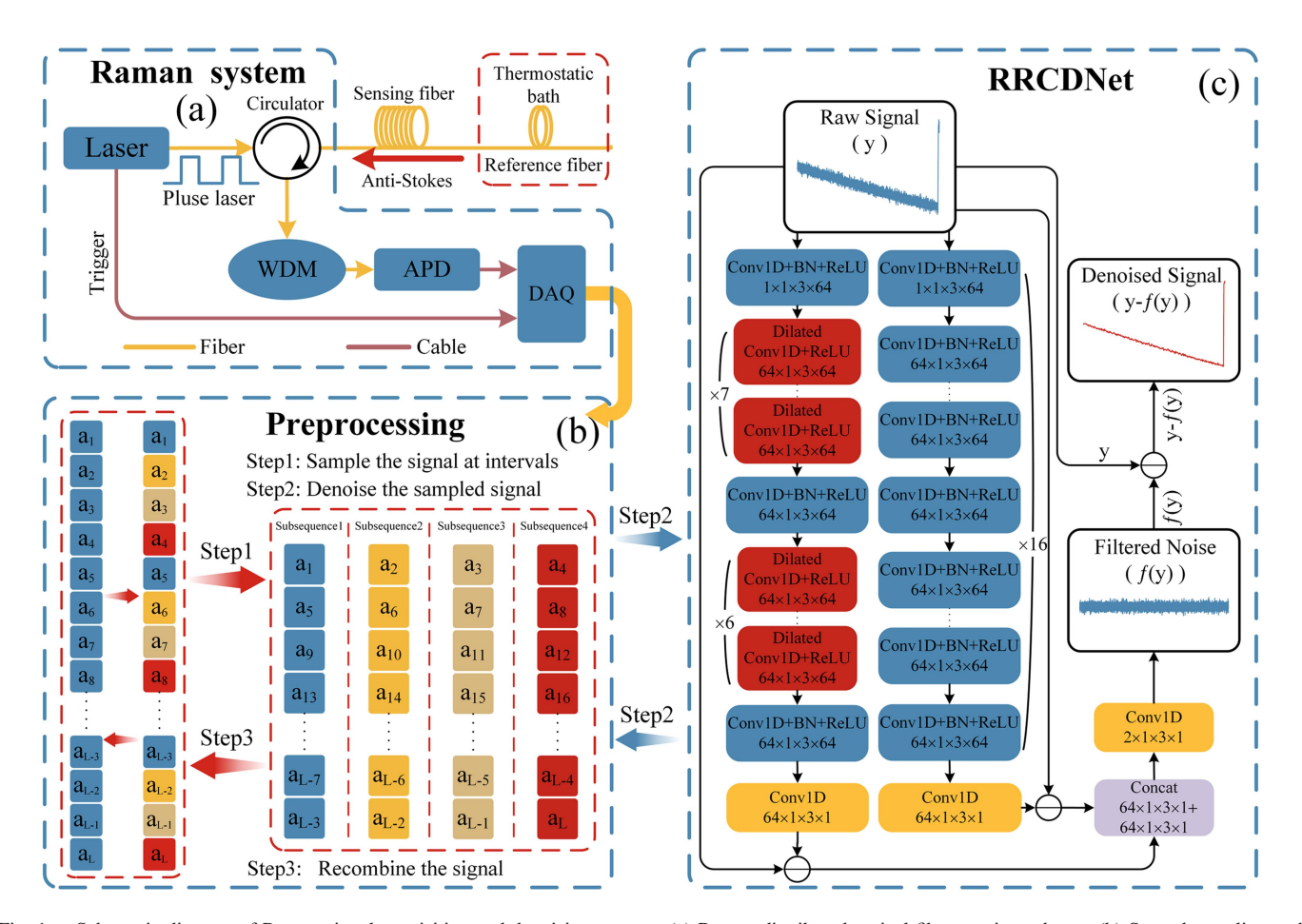


Fig. 1. Schematic diagram of Raman signal acquisition and denoising process. (a) Raman distributed optical fiber sensing scheme. (b) Spaced sampling and recombining the sub-signal sequence into the complete signal. (c) The Raman residual composite dual-convolutional neural network (RRCDNet).

of RRCDNet in suppressing low-frequency noise. In order to prevent the loss of information in the rising or falling edge of a signal, it is crucial that the maximum number of interval points during the interval sampling preprocessing is limited to less than the number of sampling points within the rising or falling edge. The signals, which have a sample rate of 1G or higher, undergo a sequential processing procedure consisting of three steps: 8-divided sampling and denoising, followed by 4-divided sampling and denoising, and finally direct denoising (RRCDNet<sub>841</sub>). Use RRCDNet<sub>41</sub> to process signals with a sampling rate of about 300M, and RRCDNet<sub>21</sub> to process signals with a sampling rate of about 100M or less.

# C. RRCDNet

The CNN-based network RRCDNet (as shown in Fig. 1(c)) was proposed to denoise the Raman distributed optical fiber sensing signal and achieve better temperature precision.

*Principle:* The technologies used in RRCDNet are as follows: To begin, residual learning was employed in RRCDNet to handle the issue of network degradation that occurs as the neural network deepens [46]. Residual learning also combined extracted features and the input of numerous stack layers as the current layer's input, which could alleviate the vanishing or exploding problem, and gives RRCDNet the ability to extend to deeper

levels. Second, batch normalization (BN) [47] was employed to slow down the internal covariate shift phenomenon that occurs during neural network training. Third, dilated convolution [48] was employed to allow RRCDNet to get a broader perceptual field while utilizing fewer network layers and overcome the problem of traditional CNNs using pooling procedures and increasing depth to obtain additional signal features, which leads to loss of Raman distributed fiber sensing signal information and degradation of network performance. Final, RRCDNet employs Kaiming initialization, a suitable initialization approach for the ReLU activation function [49], to address the decreasing gradient in backward propagation.

*Method:* The structure of RRCDNet are as follows: RRCDNet has two feature extraction networks to extract different features that are complementary in the denoising work. The first feature extraction network (right network) has a depth of 17. It is made up of two sorts of layers: Conv + BN + ReLU (convolution, batch normalization, and rectified linear units are performed sequentially) and Conv. Layers 1-16 are Conv + BN + ReLU, while layer sixteenth is Conv. Except for the first and final levels, each layer is  $64 \times 1 \times 3 \times 64$  (The first "64" means the size of the in-channel, and the final "64" means out-channel, while the " $1 \times 3$ " means kernel size) in size. The first and final layers are  $1 \times 1 \times 3 \times 64$  and  $64 \times 1 \times 3 \times 1$  respectively, and the padding is 1. Furthermore, the first feature extraction network

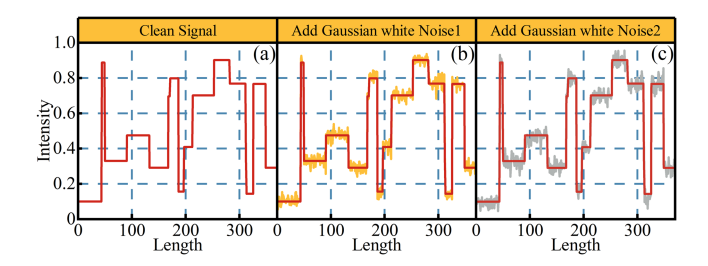


Fig. 2. (a) The clean synthesized signal without any noise. (b) the raw synthesized signal composed of clean synthesized signal and Gaussian noise. (c) Another raw synthesized signal composed of clean synthesized signal and Gaussian noise different from that in (b).

has a receptive field of 35. The second feature extraction network (left network) has a depth of 17, and uses Conv + BN + ReLUin its first, ninth, and sixteenth layers. Dilated convolutions + ReLU are used in layers 2–8 and 10–15. The dilation factor for the dilated convolutions is 2. The final layer is only Conv. Adding BN layers ensures that the distributions of the two sub-networks' outputs remain consistent. The left network achieves a larger receptive field of 61 by using dilated convolution, resulting in the ability to reconstruct the denoised signal using a wider range of input sequences. However, this approach sacrifices the continuity and completeness of the data, resulting in a loss of detail in the reconstructed signal. In contrast, the right network uses a conventional convolutional neural network architecture, with a receptive field of 35 for the equivalent number of layers. This configuration allows the network to effectively capture intricate details within the data during the processing stage, outperforming the left network. The collaboration between the two networks enhances the field of "vision" of RRCDNet, resulting in both extensive and comprehensive coverage. The symbol represents the use of residual learning (RL) in RRCDNet. Concat is used to cascade two RRCDNet subnetworks through their channels. For example, if the output channels of each of the above two sub-networks are 1 (64  $\times$  1  $\times$  3  $\times$  1), then by cascading operation, their combined output channel is 2 (64  $\times$  $1 \times 3 \times 1 + 64 \times 1 \times 3 \times 1$ ). The number of parameters in RRCDNet is about 370k, compared to 220k in 1DDCNN, and all of them are smaller neural network models.

Training sets: The training set has a substantial effect on the neural network's ultimate performance, and here synthetic datasets were used to make it easier to get a dataset. Previously, it was thought that a noise-to-clean (Noise2Clean) (from Fig. 2(b) to (a)) dataset had to be used to train the network's denoising ability, but recent research has shown that the same effect can be achieved with a noise-to-noise (Noise2Noise) (from Fig. 2(b) to 2(c)) dataset [50], which points the way to creating better datasets using real Raman signals. But here, we still use Noise2Clean to build the datasets. As shown in Fig. 2(a), a random signal was generated with an amplitude between 0 and 1 and a random length (time) of 1 to 50 points for each amplitude to simulate the decay of the Raman distributed fiber sensing signal with distance and the intensity change in the variable temperature region. The total length of each signal is 10000 points as a clean synthesized signal. The main noise component of the Raman distributed fiber sensing signal is additive Gaussian white noise. Noise with SNR ranging from 20 dB to 37 dB was generated referencing clean synthesized signal by adding Gaussian noise to produce raw synthesized signal (as shown in Fig. 2(b)). Adding Gaussian noise with multiple SNRs within a certain range to the training set improves the robustness of RRCDNet. The clean synthesized signal was set as label data  $x_{train}$ , the raw synthesized signal was set as input data  $y_{train}$ . And normalize  $y_{train}$  by [0,1] and then scale  $x_{train}$  by the same proportion. 5000 sets of the aforementioned data were generated, with 4500 sets serving as the training set and 500 sets serving as the test set.

Training: Training RRCDNet uses  $y_{train}$  as input data and  $x_{train}$  as label data. The training data sets for RRCDNet is  $\{x_{train}, y_{train}\}_{j=1}^{N}$ . The RL structure of RRCDNet becomes a model that can predict the residual of y, can be represented as f. Through an examination of the neural network's architecture and the mathematical connections inherent within it, it is possible to ascertain that the output of the residual block is filtered noise f(y), which could be represented as v'. Then the denoised signal can be expressed as  $x'_{RRCDNET} = y - f(y)$ . RRCDNet uses the Adam [51] optimizer to minimize the mean-square error loss function (1) to train the network with a learning rate of 0.0003. The batch is 32, and the epochs are 128. Where  $\theta$  indicates the parameters of the RRCDNet model, N is the batch size, Raw signal  $y_i$  and the clean signal corresponding to it  $x_i$  are one set of training sets. And  $\|\cdot\|_F$  stands for Frobenius norm.

$$loss(\theta) = \frac{1}{2N} \sum_{i=1}^{N} \|y_i - f(y_i, \theta) - x_i\|_F^2.$$
 (1)

The structural and technical advantages of RRCDNet are fourfold: First, it harvests more information by employing two sub-networks rather than increasing the depth to increase denoising performance. Second, it employs BN to address the internal covariate shift issue. Third, it employs RL to avoid gradient disappearance or explosion. Finally, it uses dilated convolution to reduce computational cost. The experimental results show that RRCDNet outperforms the normal wavelet denoising algorithm and the current neural network denoising algorithm 1DDCNN.

## D. Metrics for Denoising Performance

Denoising performance of algorithms are evaluated by the following metrics: The average noise and structural similarity index measure (SSIM) evaluate denoising performance from the perspective of Raman distributed fiber sensing signals. The RMSE, smoothness, and peak-to-peak evaluate denoising performance from the perspective of temperature curves. And SSIM and denoising are calculated based on [0, 1] normalization (as (2) and (3)). In practical applications, it is not possible to obtain an absolutely clean and noise-free signal, the SNR is usually derived from estimates, whereas RRCDNet and 1DDCNN are themselves powerful denoising methods, and estimating the SNR is meaningless. Therefore, SNR and its associated metrics are not used to evaluate the efficacy of denoising in this paper

TABLE I PARAMETERS FOR THE DENOISING ALGORITHMS

Parameters	Symbol
Raw signal (acquisition from Raman distributed optical fiber sensors system)	у
Ideal spontaneous Raman scattering (without any noise)	x
The all noise of Real signal (All the noise of $y$ )	υ
Denoised-Signal ( y processed by one denoising method)	x'
Filtered-noise (Noise filtered by one denoising method)	v'
Raw signals in synthesized data (label data)	$y_{train}$
Clean signals in synthesized data (input data)	$x_{train}$
Additive Gaussian white noise in Synthetic Data	$v_{train}$
Three-layer decomposition and reconstruction using db3 wavelet base	WD3
Four-layer decomposition and reconstruction using db3 wavelet base	WD4
Denoised signal using WD4	$x'_{WD4}$
Filtered-noise using WD4	${v'}_{WD4}$
Temperature curve demodulated using $x'_{WD4}$	$T(x'_{WD4})$

[39], [43]. The meaning of the parameters is shown in Table I.

$$y_{normal}(i) = \frac{y(i) - \min[y(i)]}{\max[y(i)] - \min[y(i)]}.$$
 (2)

$$v_{normal}(i) = \frac{v(i)}{\max[y(i)] - \min[y(i)]}.$$
 (3)

Average noise is used to evaluate effective signal removal of the denoising algorithms. The primary component of  $\upsilon$  is regarded as additive Gaussian white noise, and its average value is regarded as zero; if not, it is considered that this denoising algorithm removes the effect signal. The average value of the local noise can be calculated as (4). Where l is the length of the local noise data, and L is the total length of the noise data. The closer the metric is to zero, the better the denoising performance.

average noise = 
$$\sum_{i=0}^{L-l} \left| \frac{\sum_{j=1}^{l} v'_{i+j}}{l} \right| / L - l.$$
 (4)

SSIM [45] was introduced from the field of image processing for the first time in the Raman distributed optical fiber sensors denoising task. The effective signal x is generally considered to be clean and smooth without burr, and the structural characteristics of y are mainly determined by amplitude and fluctuation of v. The SSIM compares the structural differences between filtered-noise v' and raw signal y, and the closer the value of SSIM (5) is to 1, the better the denoising performance. And  $\alpha$ ,  $\beta$ ,  $\gamma$  denote the relative importance of each metric. Where l(y, y - v') (6) measures the intensity similarity of raw signal y and denoised signal x', and evaluate effective signal removal during denoising process. We can simply interpret  $\mu_y$  as the local mean of y, with  $C_1 = (0.01)^2$  ensuring that the denominator is greater than zero. c(y, v') (7) measures the amplitude similarity of y and v'. The symbol  $\sigma_y$  is a metric for quantifying the extent and variability of the y values relative to the mean value  $\mu_y$ . In a physical context, this metric can be interpreted as the size

of the noise. The term  $C_2=(0.03)^2$  is included to ensure that the denominator is always greater than zero. And s(y,v') (8) measures the fluctuation similarity of y and v'. (8) quantifies the similarity of fluctuations between the variables y and v'. The symbol  $\sigma_{yv'}$  represents the correlation between y and v', which can be interpreted as the level of synchronisation between the upward and down-ward fluctuations of the original signal and the filtered noise. The term  $C_3=C_2$  /2 is included to ensure that the denominator of the equation is always greater than zero. The values of  $\alpha=1$ ,  $\beta=1$ , and  $\gamma=1$  are employed to signify that the factors l, c, and s carry equal significance in the computation of the SSIM. The  $\omega$  is the Gaussian sliding window of length 25, in which the standard deviation is 3.6 and the sum is 1.

$$SSIM(y, v') = [l(y, y - v')]^{\alpha} \cdot [c(y, v')]^{\beta} \cdot [s(y, v')]^{\gamma}.$$
 (5)

$$l(y, y - v') = \frac{2\mu_y \mu_{y-v'} + C_1}{\mu_y^2 + \mu_{y-v'}^2 + C_1}.$$
 (6)

$$c(y, v') = \frac{2\sigma_y \sigma_{v'} + C_2}{\sigma_y^2 + \sigma_{v'}^2 + C_2}.$$
 (7)

$$s(y,v') = \frac{\sigma_{yv'} + C_3}{\sigma_y\sigma_{v'} + C_3}.$$
 (8)

$$\mu_y = \sum_{i=1}^L \omega_i y_i. \tag{9}$$

$$\sigma_y = \left(\sum_{i=1}^L \omega_i \left(y_i - \mu_y\right)^2\right)^{\frac{1}{2}}.$$
 (10)

$$\sigma_{yv'} = \sum_{i=1}^{L} \omega_i (y_i - \mu_y) (v' - \mu_{v'}).$$
 (11)

Smoothness can reflect the precision of the temperature curve as (12). Where  $T_i$  is the i-th point on a temperature curve of length L. The closer the metric is to zero, the better the denoising performance.

$$smoothness = \sum_{i=1}^{L-1} |T_i - T_{i+1}| / (L-1).$$
 (12)

### III. EXPERIMENT

#### A. Raman Distributed Optical Fiber Sensing System

The denoising ability of RRCDNet was tested using the genuine signal obtained by the Raman distributed optical fiber sensors system. The Raman system employed in this work is shown in Fig. 1(a). The system comprised a distributed feedback laser, circulator, WDM, high-speed data acquisition card, and APD. The pulsed laser source had a wavelength of 1550 nm and a repetition rate of 6 kHz. The sensing fiber (graded-index multimode, 62.5/125, MMF) was launched with pulses having a peak optical power of 15 W. The Raman anti-Stokes signal is filtered out using WDM and then supplied to the APD, which generates the electrical signal. The electrical signals of Raman distributed optical fiber sensors were then gathered by a data acquisition card and sent to a computer to perform the processes

of denoising the Raman distributed fiber sensing signal, demodulating the temperature, and denoising the temperature curve sequentially.

## B. Temperature Demodulation

Raman distributed optical fiber sensors that demodulates the temperature using the principle that the anti-Stokes light in the spontaneous Raman backscattering effect is sensitive to temperature. Among the various methods, the single-way demodulation of the anti-Stokes light (as (13)) was selected [52].

$$T(L) = h\Delta\nu / k \ln \left[ \frac{\exp(h\Delta\nu/kT_0) - 1}{\Phi_{AS}(T, L)} \cdot \Phi_{AS}(T_0, L) + 1 \right].$$
(13)

Where  $\Phi_{AS}$  represents the Anti-Stokes flux, which can be replaced by the voltage amplitude of the APD output  $U_{AS}$ . And L is the length of the scattering location from the fiber port. And  $\Phi_{AS}(T_0,L)$  represents the Anti-Stokes flux at a known temperature  $T_0$  (in Kelvin), h is Planck's constant,  $\Delta \nu$  is the difference between the upper and lower energy levels of the Raman scattering spectrum, k is the Boltzmann constant, and  $h\Delta\nu/k=634$ . From the above equation, it can be seen that the SNR of the SpRS signal  $\Phi_{AS}$  of Raman distributed optical fiber sensors is directly determines the temperature precision.

## IV. EXPERIMENTAL RESULTS AND DISCUSSION

This section compares the advantages and disadvantages of three denoising algorithms, WD4, 1DDCNN, and RRCDNet. To validate the validity of the evaluation metrics, WD3 is compared to WD4 under these metrics. The method of spectral analysis is used to analyze the noise filtering ability of the denoising algorithms for different frequencies and characteristics.

## A. Denoising Performance Analysis in Time Domain

To verify the robustness of the denoising algorithms, two sets of Raman distributed fiber sensing signals were collected with a temperature zone of 60 °C at the end of the fiber, averaged five thousand and ten thousand times respectively. And WD4, 1DDCNN, RRCDNet the three denoising algorithms are compared (as shown in Fig. 3). As shown in Table II and Fig. 3: First, Average noise and SSIM are employed to quantify the performance of the denoising algorithms. And the RRCDNet has an excellent performance among the average noise and SSIM evaluation metrics. For the average noise metric, RRCDNet shows inferior performance compared to wavelet denoising. This is due to the fact that RRCDNet tends to filter out a larger amount of noise, resulting in a bigger loss of the effective signal compared to wavelet denoising. However, as the same kind of denoising method, which use the same denoising principle, RRCDNet is better than 1DDCNN in the metric of average noise and has a lower remove on the effective signal. 1DDCNN removes effective signal more severely, causing the Raman distributed fiber sensing signal to shift significantly compared to the raw data, WD4 and RRCDNet (as shown in Fig. 3(c2) and (d2)), resulting the temperature accuracy to decline, whereas this phenomenon is not obvious for RRCDNet. Second, both

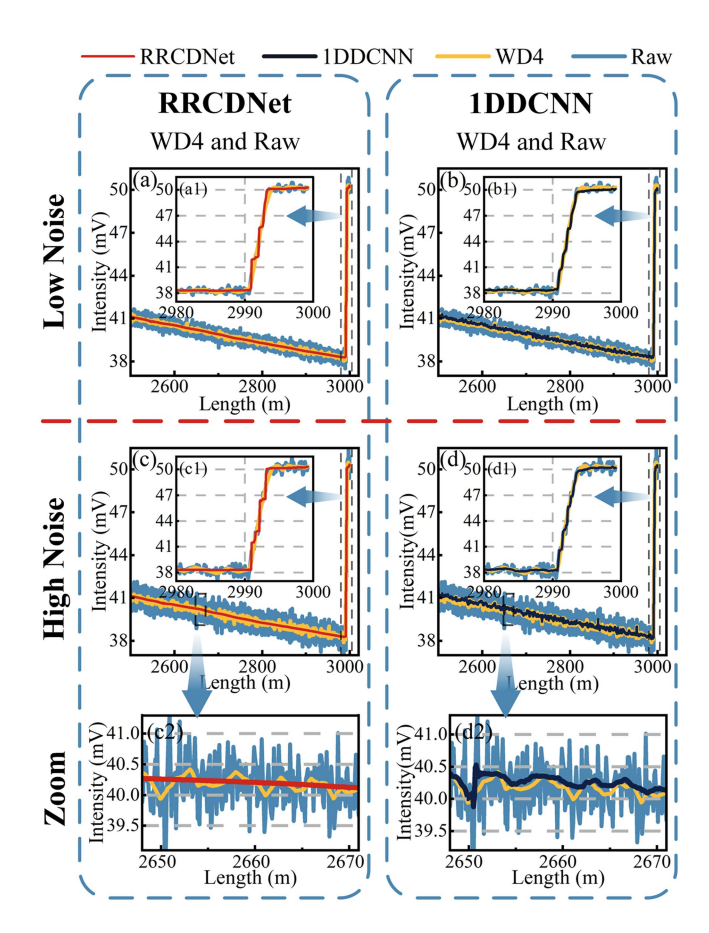


Fig. 3. Raman distributed fiber sensing signal processed by multiple denoising methods The (a) and (c) displays raw Raman distributed fiber sensing signal y averaged 10000 times and 5000 times, and its denoised signal processed by RRCDNet and WD4 respectively; The (b) and (d) displays raw Raman signal y averaged 10000 times and 5000 times, and its denoised signal processed by 1DDCNN and WD4 respectively; The (c2) and (d2) are local zooms, and it can be clearly seen that 1DDCNN's processing causes the Raman distributed fiber sensing signal to shift. The (a1), (b1), (c1), and (d1) are local zooms, and it can be clearly seen that neither RRCDNet nor 1DDCNN change the spatial resolution of the system during the processing of the signal.

1DDCNN and RRCDNet did not degrade spatial resolution in the of denoising process (as shown in Fig. 3(a1) and (b1)). Thus, the threshold in the WD4 denoising technique should be lowered so that the reconstructed signal also does not degrade the spatial resolution. Finally, compared with the processing of the low-noise Raman distributed optical fiber sensor signals after a cumulative average of 10000 times, RRCDNet still performs well in the task of processing the high-noise Raman signals with a cumulative average of 5000 times, proving its robustness.

Demodulating the Raman distributed fiber sensing signals into temperature curves (as shown in Fig. 4). The performance of the denoising algorithms in the temperature curve is measured using three metrics: smoothness, RMSE, and peak-to-peak (as shown in Table III). And Table III shows that RRCDNet's metrics are the best for all denoising algorithms with both high and low noise signals. In particular, the smoothness of the temperature curve of the high-noise signal averaged 5000 times is improved from 1.478 to 0.0051, an improvement of about 300 times and more than two orders of magnitude. The temperature precision greatly improved by a factor of 100 from 7.57 °C to 0.06 °C

TABLE II

EVALUATION METRICS FOR RAMAN DISTRIBUTED FIBER SENSING SIGNAL
PROCESSED BY WD3, WD4, 1DDCNN, AND RRCDNET UNDER DIFFERENT
NOISE AMPLITUDE

Noise Level	Filtered-Noise	Average Noise	SSIM
	$v'_{WD3}$	$0.551 \times 10^{-3}$	0.943
Average	${v'}_{WD4}$	$0.645 \times 10^{-3}$	0.958
10000	${v'}_{1DDCNN}$	$4.353 \times 10^{-3}$	0.961
	${v'}_{RRCDNET}$	$2.024 \times 10^{-3}$	0.962
	$v'_{WD3}$	0.621×10 <sup>-3</sup>	0.951
Average	${v'}_{WD4}$	$0.755 \times 10^{-3}$	0.966
5000	${v'}_{1DDCNN}$	$4.484 \times 10^{-3}$	0.969
	$v'_{RRCDNET}$	$2.115 \times 10^{-3}$	0.972

Bold text indicates an algorithm that has the best performance for a given metric.

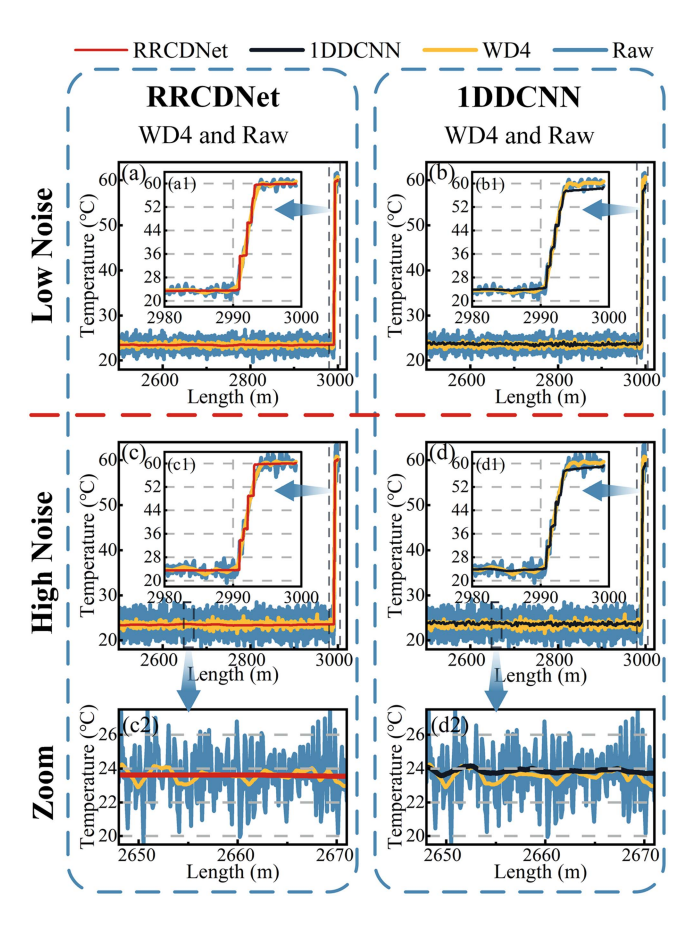


Fig. 4. Temperature curves were demodulated by Raman distributed fiber sensing signal with different noise amplitude and processed by various denoising methods.

peak-to-peak ( $\pm 0.03$  °C), in three kilometers of high noise signal averaged 5000 times. And the removal of the effective signal caused by RRCDNet was not severe enough to cause the visible temperature curve to drift as in 1DDCNN (as shown in Fig. 4(c2) and (d2)). The trained RRCDNet processes Raman signals end-to-end in about 0.3s without requiring manual parameter adjustments, hardware modifications, or other degradation of performance metrics, and is one of the best denoising algorithms among our known methods [44].

TABLE III

EVALUATION METRICS FOR TEMPERATURE CURVE PROCESSED BY WD3, WD4, 1DDCNN, AND RRCDNET UNDER DIFFERENT NOISE AMPLITUDE

Noise Level	Demodulation Temperature	Smoothness	RMSE	peak-to- peak
Average 10000	T(y)	$5.744 \times 10^{-1}$	$9.29 \times 10^{-1}$	4.451
	$T(x'_{WD3})$	$0.955 \times 10^{-1}$	$4.19 \times 10^{-1}$	1.846
	$T(x'_{WD4})$	$0.381 \times 10^{-1}$	$2.94 \times 10^{-1}$	1.090
	$T(x'_{1DDCNN})$	$0.153 \times 10^{-1}$	$1.83 \times 10^{-1}$	0.426
	$T(x'_{RRCDNET})$	$0.049 \times 10^{-1}$	$1.20 \times 10^{-1}$	0.053
Average 5000	T(y)	14.781×10 <sup>-1</sup>	15.11×10 <sup>-1</sup>	7.569
	$T(x'_{WD3})$	$1.323 \times 10^{-1}$	$5.99 \times 10^{-1}$	2.648
	$T(x'_{WD4})$	$0.597 \times 10^{-1}$	$4.34 \times 10^{-1}$	1.650
	$T(x'_{1DDCNN})$	$0.175 \times 10^{-1}$	$2.19 \times 10^{-1}$	0.535
	$T(x'_{RRCDNET})$	$0.051\times10^{-1}$	1.29×10 <sup>-1</sup>	0.061
D 11.	P - 1 - 24 - 4	. 1 . 1		

Bold text indicates an algorithm that has the best performance for a given metric.

TABLE IV
PROCESSING TIME OF DIFFERENT DENOISING ALGORITHMS

Denoising Algorithm	RRCDNet <sub>841</sub>	1DDCNN	WD
Time (s)	0.291	0.005	0.015

The experimental results show that all three methods are fast denoising algorithms with real-time performance and RRCDNet<sub>841</sub> took the longest due to its most complex computations.

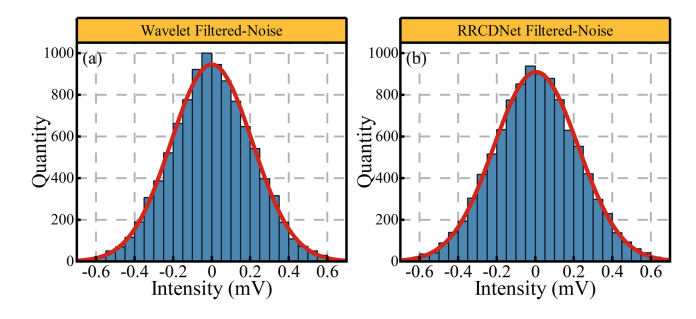


Fig. 5. (a) Amplitude distribution histogram of noise filtered by WD4. (b) Amplitude distribution histogram of noise filtered by RRCDNet.

The amplitude distribution of the noise characteristics of the Raman signal is qualitatively analyzed to inform the construction of the RRCDNet's training set. The amplitude distribution of the noise filtered by wavelet denoising was examined (as shown in Fig. 5(a)), and it was found that the noise of the signal is Gaussian distributed. And combined with Fig. 6(a1), the analysis shows that the noise of the Raman signal approximates additive Gaussian white noise.

## B. Denoising Performance Analysis in Frequency Domain

The power spectral density was used to qualitatively analyze the denoising ability of RRCDNet. It is often assumed that high frequency and low energy components mostly belong to noise, while low frequency and high energy components mostly belong to effective signals. The raw signal has some energy belonging to the noise (as shown in Fig. 6(a0)) in the low frequency region, and methods have been suggested in previous studies

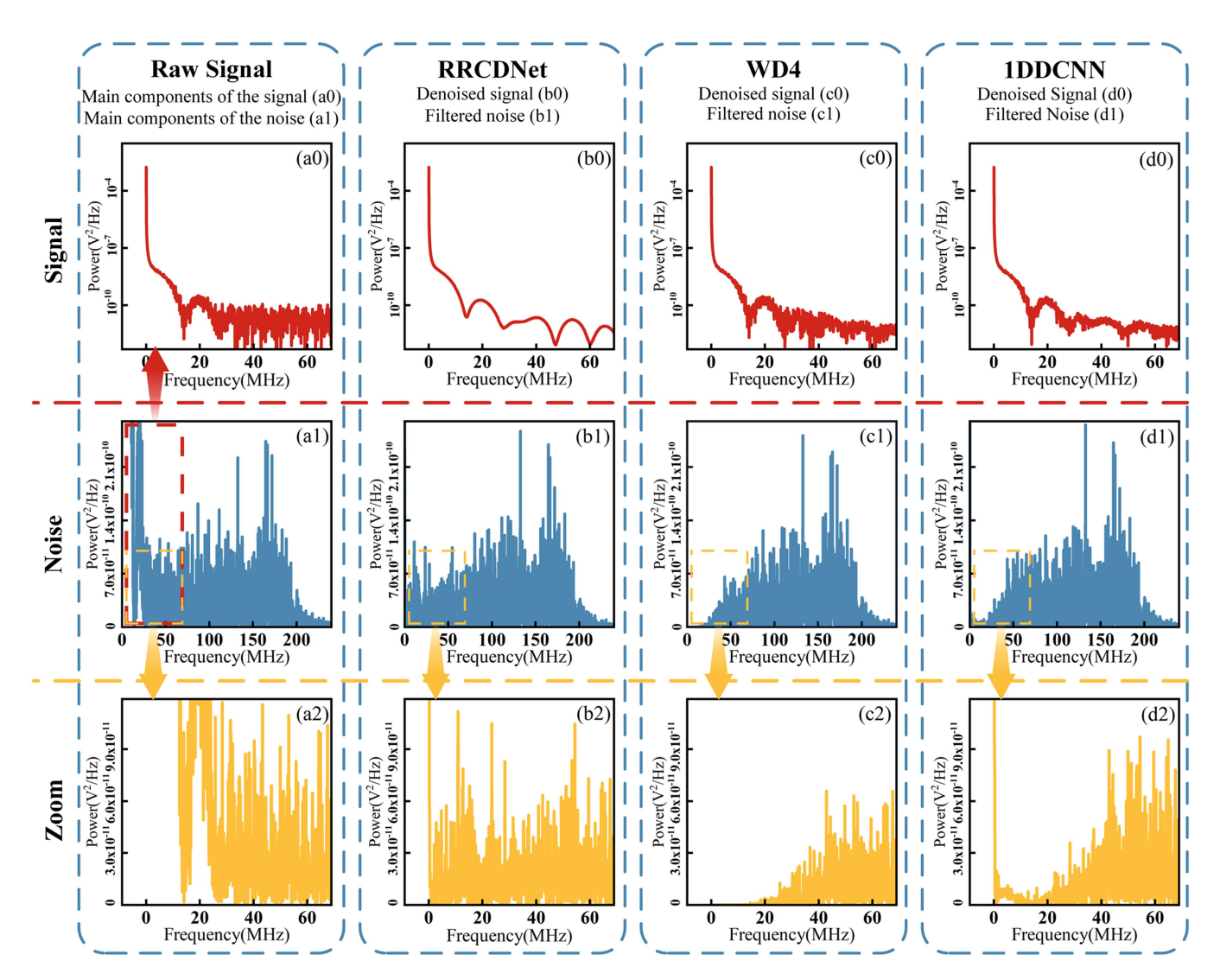


Fig. 6. Spectral analysis of denoised signal and filtered noise processed by various denoising algorithms. (a0) The power distribution of the signal in the low frequency range, and it is generally considered that most of the energy in the low frequency range belongs to the signal and only a small portion of the energy belongs to the noise. (b0) The power distribution of the signal denoised by RRCDNet in the low-frequency domain shows that RRCDNet denoises low-frequency noise very well. (c0) The power distribution of the signal denoised by WD4 in the low-frequency domain shows that the WD4 has a poor ability to remove low-frequency noise. (d0) The power distribution of 1DDCNN denoised signals in the low-frequency domain, which shows the denoising ability of 1DDCNN on low-frequency noise is between the two methods mentioned above. (a1) The power distribution of the raw signal in the entire frequency domain, which can be used to compare the rate removal ability of different denoising methods for different frequency noise. (b1), (c1), and (d1) Power distribution of the signal denoised by RRCDNet, WD4, or 1DDCNN, respectively, in the whole frequency domain. (a2), (b2), (c2), and (d2) The localized enlarged images of (a1), (b1), (c1), or (d1), respectively, show the excellent filtering ability of RRCDNet for low frequency noise.

WD4 and 1DDCNN have limited ability for the noise in the low frequency region (as shown in Fig. 6(c0) and (d0)), while the RRCDNet can suppress the low-frequency noise (as shown in Fig. 6(b0)) very well. From the whole frequency domain (as shown in Fig. 6(a1)), although the previous denoising methods can suppress the high-frequency noise (as shown in Fig. 6(c1) and (d1)) in the Raman signal, they have poor suppression ability for the low-frequency noise, which is the main reason why the temperature profile still fluctuates significantly in the time domain. And RRCDNet can suppress the low-frequency noise (as shown in Fig. 6(b1)) very well from making the temperature profile in the time domain smoother than ever before and achieving unprecedented temperature precision. Similar to the quantitative analysis in the time domain, the qualitative analysis

in the frequency domain also confirms the excellent denoising performance of RRCDNet.

# C. Robustness Testing

To show the denoising ability of RRCDNet in different cases, we used different Raman sensing systems with approximately 3.8km of optical fiber to acquire Raman signals using 100M, 250M, and 1G sampling rates (as shown in Fig.7). The 100M signal was processed by RRCDNet<sub>21</sub>(2-divided sampling and denoising, followed by direct denoising), the 250M signal by RRCDNet<sub>41</sub>, and the 1G signal by RRCDNet<sub>841</sub>(8-divided sampling and denoising, followed by 4-divided sampling and denoising, and finally direct denoising). RRCDNet still has

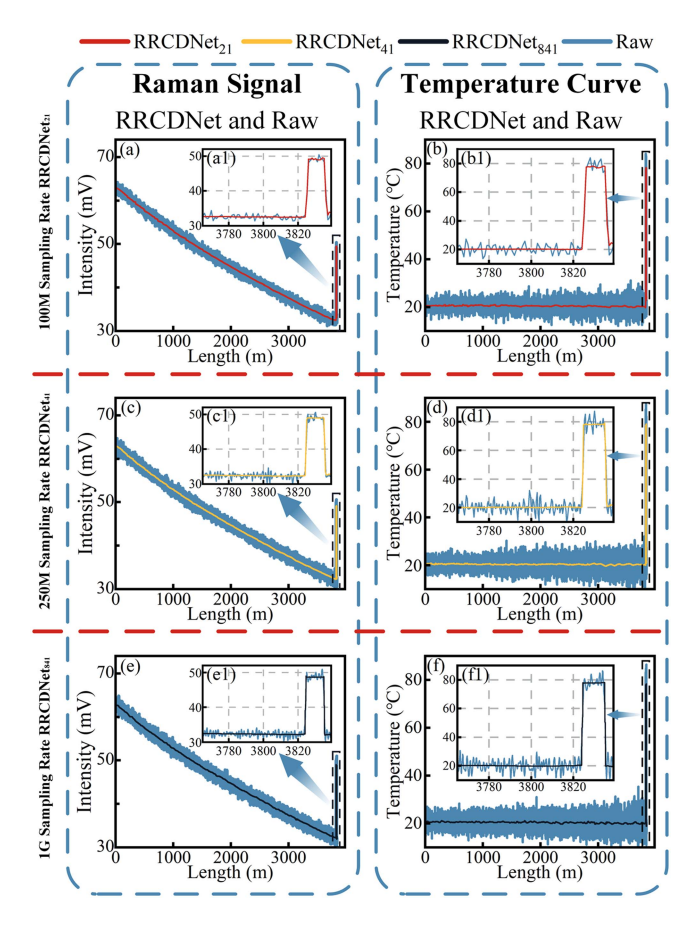


Fig. 7. Results of RRCDNet processing the signal at different sampling rates and demodulating them into temperature curves. The (a) displays raw Raman distributed fiber sensing signal y with a sampling rate of 100M, averaged 5000 times, and its denoised signal processed by RRCDNet<sub>21</sub>. (b) displays the results of demodulating them separately into temperature curves; The (c) displays raw Raman distributed fiber sensing signal y with a sampling rate of 250M, averaged 5000 times, and its denoised signal processed by RRCDNet<sub>41</sub>. (d) displays the results of demodulating them separately into temperature curves; The (e) displays raw Raman distributed fiber sensing signal y with a sampling rate of 1G, averaged 5000 times, and its denoised signal processed by RRCDNet<sub>841</sub>. (f) displays the results of demodulating them separately into temperature curves; (a1), (b1), (c1), (d1), (e1), and (f1) are localized zoomed-in figures.

excellent noise suppression under different system states. The aforementioned experiment also demonstrated the soundness of the suggested sampling intervals in the preprocessing approach for Raman signals with varying sampling rates.

## D. Ablation Study

A series of ablation experiments were performed on the relevant structures within RRCDNet (as shown in Fig. 8). The structure of right network (as shown in Fig. 8(a1)) and left network (as shown in Fig. 8(b1)) does not converge well (as shown in Fig. 8(a2) and (b2)) in process of learning the denoising task due to the oversimplification and irrationality of the structure. The last residual connection structure is eliminated (as shown in Fig. 8(e1)), and the entire network is not designed as a residual block for predicting signal's noise. Instead, the clean signal is directly reconstructed and outputted (as shown in Fig. 8(e1)). As shown in Fig. 8(e2), the network convergence

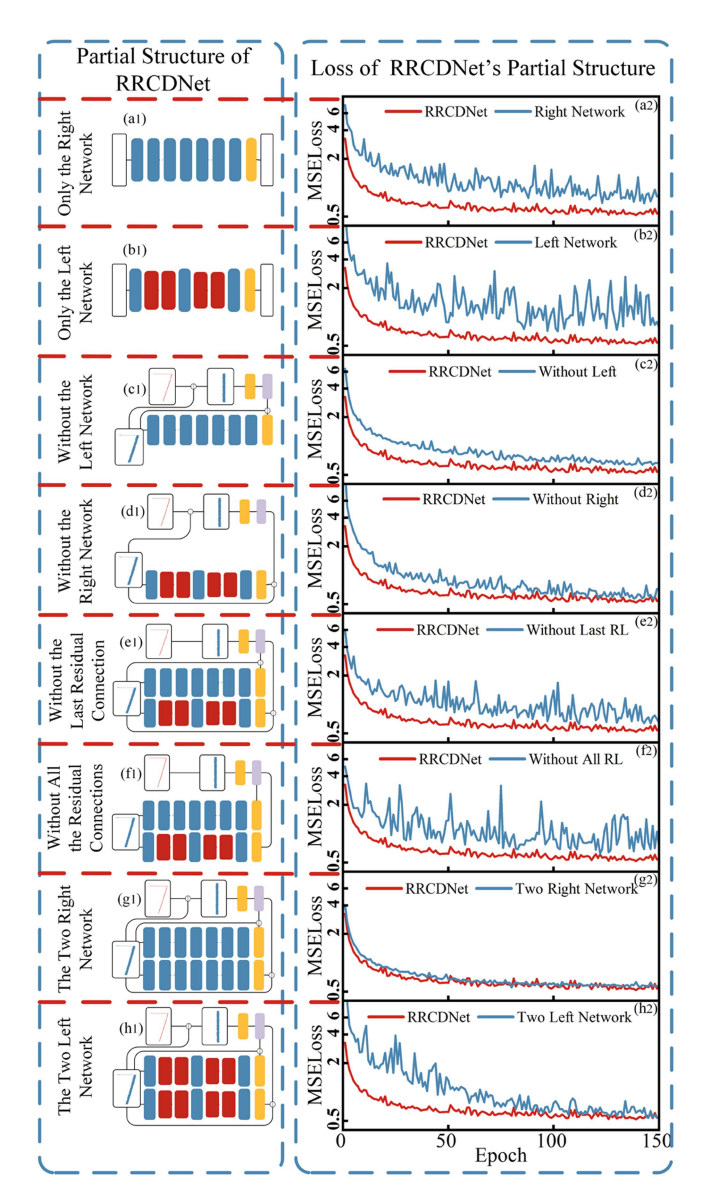


Fig. 8. Partial structure of RRCDNet and corresponding losses. The (a1) displays the structure of right network in RRCDNet; And (a2) displays the losses of the right network and RRCDNet respectively; The (b1) displays the structure of left network in RRCDNet; The (c1) displays the structure of RRCDNet without the left network; The (d1) displays the structure of RRCDNet without the Right network; The (e1) displays the structure of RRCDNet without the last residual connection; The (f1) displays the structure of RRCDNet without the all residual connection; The (g1) displays the structure of RRCDNet which change the Left network into the Right network; The (h1) RRCDNet which change the Right network into the Left network.

deteriorates, which leads to a decrease in denoising ability. This experiment demonstrates the importance of using the residual connection structure in RRCDNet, which first filters out the noise and then reconstructs the signal, rather than reconstructing the signal directly. The structure (as shown in Fig. 8(f1)) removes all the residual connectivity in RRCDNet, and its performance degrades further (as shown in Fig. 8(f2)). It is proved that the structure of residual connections is equally indispensable in the network. The experiment (as shown in Fig. 8) provides that all components within RRCDNet are indispensable and mutually reliant in the task of denoising.

## V. CONCLUSION

The RRCDNet, a novel CNN-based denoising network that uses advanced deep learning techniques to achieve superior denoising performance, is reported in this paper. RRCDNet uses the residual learning and the dual network-concat structure to greatly improve the learning ability of neural networks. And the synthetic datasets are proposed for the denoising task of Raman signals, which makes the acquisition of training sets easy. The preprocessing method of interval sampling and reconstruction enhance the low-frequency noise suppression ability of RRCD-Net. The RRCDNet-enhanced Raman distributed fiber sensing system dramatically improves the smoothness of the temperature distribution curve by approximately 300 times. And RRCDNet improves temperature precision from 7.57 °C peak-to-peak to  $0.06\,^{\circ}\text{C}$  ( $\pm 0.03\,^{\circ}\text{C}$ ), a more than 100-fold improvement, with a processing time of about 0.3 seconds. As far as we know, this is the best temperature precision reported in the Raman distributed optical fiber sensing scheme. Unlike other schemes of improving signal-to-noise ratio, RRCDNet does not require manual adjustment of parameters, increase system complexity, or degrade other performance metrics of Raman distributed fiber sensors. RRCDNet's comprehensive capabilities are extremely impressive.

Furthermore, the potential of RRCDNet extends beyond denoising Raman distributed fiber sensor signals. We believe that after training set modification and migration learning, RRCDNet could be applied to other distributed fiber sensors.

# REFERENCES

- [1] J. Li and M. Zhang, "Physics and applications of Raman distributed optical fiber sensing," *Light Sci. Appl.*, vol. 11, no. 1, May 2022, Art. no. 128, doi: 10.1038/s41377-022-00811-x.
- [2] H. He et al., "Integrated sensing and communication in an optical fibre," *Light Sci. Appl.*, vol. 12, no. 1, Jan. 2023, Art. no. 25, doi: 10.1038/s41377-022-01067-1.
- [3] F. Yang, F. Gyger, and L. Thévenaz, "Intense Brillouin amplification in gas using hollow-core waveguides," *Nature Photon.*, vol. 14, no. 11, pp. 700–708, Nov. 2020, doi: 10.1038/s41566-020-0676-z.
- [4] E. F. Williams et al., "Distributed sensing of microseisms and teleseisms with submarine dark fibers," *Nature Commun.*, vol. 10, no. 1, Dec. 2019, Art. no. 5778, doi: 10.1038/s41467-019-13262-7.
- [5] Z. Zhan et al., "Optical polarization-based seismic and water wave sensing on transoceanic cables," *Science*, vol. 371, no. 6532, pp. 931–936, Feb. 2021, doi: 10.1126/science.abe6648.
- [6] F. Muñoz and M. A. Soto, "Enhancing fibre-optic distributed acoustic sensing capabilities with blind near-field array signal processing," *Nature Commun.*, vol. 13, no. 1, Jul. 2022, Art. no. 4019, doi: 10.1038/s41467-022-31681-x.
- [7] M. A. Soto, Z. Yang, J. A. Ramírez, S. Zaslawski, and L. Thévenaz, "Evaluating measurement uncertainty in Brillouin distributed optical fibre sensors using image denoising," *Nature Commun.*, vol. 12, no. 1, Aug. 2021, Art. no. 4901, doi: 10.1038/s41467-021-25114-4.
- [8] A. Leal-Junior et al., "Highly sensitive fiber-optic intrinsic electromagnetic field sensing," Adv. Photon. Res., vol. 2, no. 1, Jan. 2021, Art. no. 2000078, doi: 10.1002/adpr.202000078.
- [9] X. Lou, Y. Feng, S. Yang, and Y. Dong, "Ultra-wide-dynamic-range gas sensing by optical pathlength multiplexed absorption spectroscopy," *Pho*ton. Res., vol. 9, no. 2, pp. 193–201, Feb. 2021, doi: 10.1364/prj.411870.
- [10] G. Bashan, H. H. Diamandi, Y. London, E. Preter, and A. Zadok, "Optomechanical time-domain reflectometry," *Nature Commun.*, vol. 9, no. 1, Jul. 2018, Art. no. 2991, doi: 10.1038/s41467-018-05404-0.
- [11] C. V. Raman and K. S. Krishnan, "A new type of secondary radiation," *Nature*, vol. 121, pp. 501–502, Jan.–Jun. 1928, doi: 10.1038/121501c0.

- [12] P. Lu et al., "Distributed optical fiber sensing: Review and perspective," Appl. Phys. Rev., vol. 6, no. 4, Dec. 2019, Art. no. 041302, doi: 10.1063/1.5113955.
- [13] A. H. Hartog, A. P. Leach, and M. P. Gold, "Distributed temperature sensing in solid-core fibres," *Electron. Lett.*, vol. 21, no. 23, pp. 1061–1062, Nov. 1985, doi: 10.1049/el:19850752.
- [14] I. Ashry et al., "A review of distributed fiber-optic sensing in the oil and gas industry," J. Lightw. Technol., vol. 40, no. 5, pp. 1407–1431, Mar. 2022, doi: 10.1109/jlt.2021.3135653.
- [15] A. Datta, H. Mamidala, D. Venkitesh, and B. Srinivasan, "Reference-free real-time power line monitoring using distributed anti-stokes Raman thermometry for smart power grids," *IEEE Sens. J.*, vol. 20, no. 13, pp. 7044–7052, Jul. 2020, doi: 10.1109/jsen.2019. 2961185
- [16] Y. Liu, X. Li, H. Li, and X. Fan, "Global temperature sensing for an operating power transformer based on Raman scattering," *Sensors*, vol. 20, no. 17, pp. 1–15, Sep. 2020, doi: 10.3390/s20174903.
- [17] J. Li et al., "Long-range Raman distributed fiber temperature sensor with early warning model for fire detection and prevention," *IEEE Sens. J.*, vol. 19, no. 10, pp. 3711–3717, May 2019, doi: 10.1109/jsen.2019.2895735.
- [18] E. Ip et al., "Using global existing fiber networks for environmental sensing," *Proc. IEEE*, vol. 110, no. 11, pp. 1853–1888, Nov. 2022, doi: 10.1109/jproc.2022.3199742.
- [19] M. Roman et al., "Temperature monitoring in the refractory lining of a continuous casting tundish using distributed optical fiber sensors," *IEEE Trans. Instrum. Meas.*, vol. 72, Nov. 2023, Art. no. 7000511, doi: 10.1109/tim.2022.3225033.
- [20] Z. Wei, J. Hu, H. He, Y. Yu, and J. Marco, "Embedded distributed temperature sensing enabled multistate joint observation of smart lithium-ion battery," *IEEE Trans. Ind. Electron.*, vol. 70, no. 1, pp. 555–565, Jan. 2023, doi: 10.1109/tie.2022.3146503.
- [21] J. Li et al., "High-accuracy distributed temperature measurement using difference sensitive-temperature compensation for Raman-based optical fiber sensing," *Opt. Exp.*, vol. 27, no. 25, pp. 36183–36196, Dec. 2019, doi: 10.1364/oe.27.036183.
- [22] H. Wu, H. Du, C. Zhao, and M. Tang, "24 km high-performance Raman distributed temperature sensing using low water peak fiber and optimized denoising neural network," *Sensors*, vol. 22, no. 6, Mar. 2022, Art. no. 2139, doi: 10.3390/s22062139.
- [23] X. Zhou et al., "Chaos Raman optical time-domain reflectometry for millimeter-level spatial resolution temperature sensing," *J. Lightw. Technol.*, vol. 39, no. 23, pp. 7529–7538, Dec. 2021, doi: 10.1109/jlt.2021.3116203.
- [24] J. P. Dakin, D. J. Pratt, G. W. Bibby, and J. N. Ross, "Distributed optical fibre Raman temperature sensor using a semiconductor light source and detector," *Electron. Lett.*, vol. 21, no. 13, pp. 569–570, Jun. 1985, doi: 10.1049/el:19850402.
- [25] N. Deng, L. Zong, H. Jiang, Y. Duan, and K. Zhang, "Challenges and enabling technologies for multi-band WDM optical networks," *J. Lightw. Technol.*, vol. 40, no. 11, pp. 3385–3394, Jun. 2022, doi: 10.1109/jlt.2022.3162725.
- [26] S. MohammadNejad and F. Aghaei, "Noise characteristics improvement of submicron InP/InGaAs avalanche photodiode for laser detection system," *Opt. Commun.*, vol. 455, Jan. 2020, Art. no. 124561, doi: 10.1016/j.optcom.2019.124561.
- [27] B. Yan et al., "Temperature accuracy and resolution improvement for a Raman distributed fiber-optics sensor by using the Rayleigh noise suppression method," *Appl. Opt.*, vol. 59, no. 1, pp. 22–27, Jan. 2020, doi: 10.1364/AO.59.000022.
- [28] H. Yao et al., "Ring-based colorless WDM-PON With Rayleigh backscattering noise mitigation," J. Opt. Commun. Netw., vol. 9, no. 1, pp. 27–35, Jan. 2017, doi: 10.1364/jocn.9.000027.
- [29] Y. S. Muanenda et al., "Advanced coding techniques for long-range Raman/BOTDA distributed strain and temperature measurements," J. Lightw. Technol., vol. 34, no. 2, pp. 342–350, Jan. 2016, doi: 10.1109/jlt.2015.2493438.
- [30] G. Yang et al., "Enhanced Raman distributed temperature sensor using a high Raman gain fiber," *IEEE Sens. J.*, vol. 21, no. 24, pp. 27518–27525, Dec. 2021, doi: 10.1109/jsen.2021.3124906.
- [31] H. Du, H. Wu, Z. Zhang, C. Zhao, Z. Zhao, and M. Tang, "Single-ended self-calibration high-accuracy Raman distributed temperature sensing based on multi-core fiber," *Opt. Exp..*, vol. 29, no. 21, pp. 34762–34769, Oct. 2021, doi: 10.1364/OE.440265.

- [32] X. Sun et al., "Genetic-optimised aperiodic code for distributed optical fibre sensors," *Nature Commun.*, vol. 11, no. 1, Nov. 2020, Art. no. 5774, doi: 10.1038/s41467-020-19201-1.
- [33] M. K. Saxena, S. D. V. S. J. Raju, R. Arya, S. V. G. Ravindranath, S. Kher, and S. M. Oak, "Optical fiber distributed temperature sensor using short term Fourier transform based simplified signal processing of Raman signals," *Measurement*, vol. 47, pp. 345–355, Jan. 2014, doi: 10.1016/j.measurement.2013.09.001.
- [34] L. Pan, K. Liu, J. Jiang, C. Ma, M. Tian, and T. Liu, "A denoising algorithm based on EEMD in Raman-based distributed temperature sensor," *IEEE Sens. J.*, vol. 17, no. 1, pp. 134–138, Jan. 2017, doi: 10.1109/jsen.2016.2623860.
- [35] S. Mallat and W. L. Hwang, "Singularity detection and processing with wavelets," *IEEE Trans. Inf. Theory*, vol. 38, no. 2, pp. 617–643, Mar. 1992, doi: 10.1109/18.119727.
- [36] M. K. Saxena et al., "Raman optical fiber distributed temperature sensor using wavelet transform based simplified signal processing of Raman backscattered signals," Opt. Laser Technol., vol. 65, pp. 14–24, Jan. 2015, doi: 10.1016/j.optlastec.2014.06.012.
- [37] L. Fan et al., "Quaternion wavelet transform and a feedforward neural network-aided intelligent distributed optical fiber sensing system," Sensors, vol. 23, no. 7, Apr. 2023, Art. no. 3637, doi: 10.3390/s23073637.
- [38] S. Lin et al., "Enhanced Raman distributed temperature sensor based on self-constructed fully connected neural network," *IEEE Sens. J.*, vol. 22, no. 16, pp. 15967–15973, Aug. 2022, doi: 10.1109/JSEN.2022.3183014.
- [39] H. Wang, Y. Wang, X. Wang, S. Wang, and T. Liu, "A novel deep-learning model for RDTS signal denoising based on down-sampling and convolutional neural network," *J. Lightw. Technol.*, vol. 40, no. 12, pp. 3647–3653, Jun. 2022, doi: 10.1109/JLT.2022.3149400.
- [40] Y. LeCun, Y. Bengio, and G. Hinton, "Deep learning," *Nature*, vol. 521, no. 7553, pp. 436–444, May 2015, doi: 10.1038/nature14539.
- [41] J. Lehtinen et al., "Noise2Noise: Learning image restoration without clean data," in *Proc. 35th Int. Conf. Mach. Learn.*, 2018, pp. 4620–4631.
- [42] Y. Dong, Q. Liu, B. Du, and L. Zhang, "Weighted feature fusion of convolutional neural network and graph attention network for hyperspectral image classification," *IEEE Trans. Image Process.*, vol. 31, no. 1, pp. 1559–1572, 2022, doi: 10.1109/TIP.2022.3144017.
- [43] Z. Zhang, H. Wu, C. Zhao, and M. Tang, "High-performance Raman distributed temperature sensing powered by deep learning," *J. Lightw. Technol.*, vol. 39, no. 2, pp. 654–659, Jan. 2021, doi: 10.1109/jlt.2020.3032150.
- [44] M. A. Soto, J. A. Ramírez, and L. Thévenaz, "Intensifying the response of distributed optical fibre sensors using 2D and 3D image restoration," *Nature Commun.*, vol. 7, Mar. 2016, Art. no. 10870, doi: 10.1038/ncomms10870.
- [45] Z. Wang, A. C. Bovik, H. R. Sheikh, and E. P. Simoncelli, "Image quality assessment: From error visibility to structural similarity," *IEEE Trans. Image Process.*, vol. 13, no. 4, pp. 600–612, Apr. 2004, doi: 10.1109/TIP.2003.819861.
- [46] K. He, X. Zhang, S. Ren, and J. Sun, "Deep residual learning for image recognition," in *Proc. IEEE Conf. Comput. Vis. Pattern Recognit.*, 2016, pp. 770–778.
- [47] Y. Wu and K. He, "Group normalization," Int. J. Comput. Vis., vol. 128, no. 3, pp. 742–755, Mar. 2020, doi: 10.1007/s11263-019-01198-w.
- [48] C. Tian, Y. Xu, and W. Zuo, "Image denoising using deep CNN with batch renormalization," *Neural Netw.*, vol. 121, pp. 461–473, Jan. 2020, doi: 10.1016/j.neunet.2019.08.022.
- [49] K. He, X. Zhang, S. Ren, and J. Sun, "Delving deep into rectifiers: Surpassing human-level performance on imagenet classification," in *Proc. IEEE Int. Conf. Comput. Vis.*, 2015, pp. 1026–1034.

- [50] A. Krull, T. O. Buchholz, and F. Jug, "Noise2void-Learning denoising from single noisy images," in *Proc. IEEE/CVF Conf. Comput. Vis. Pattern Recognit.*, 2019, pp. 2124–2132.
- [51] A. H. Khan, X. Cao, S. Li, V. N. Katsikis, and L. Liao, "BAS-ADAM: An ADAM based approach to improve the performance of beetle antennae search optimizer," *IEEE/CAA J. Automatica Sinica*, vol. 7, no. 2, pp. 461–471, Mar. 2020, doi: 10.1109/jas.2020.1003048.
- [52] J. Li, X. Zhou, Y. Xu, L. Qiao, J. Zhang, and M. Zhang, "Slope-assisted Raman distributed optical fiber sensing," *Photon. Res.*, vol. 10, no. 1, pp. 205–213, Jan. 2022, doi: 10.1364/PRJ.442352.

**Haosen Guo** is currently working toward the postgraduation degree with the Key Laboratory of Advanced Transducers and Intelligent Control System of Ministry of Education, Taiyuan University of Technology, Taiyuan, China. His research interests include distributed optical fiber sensors and neural networks.

**Jian Li** (Member, IEEE) received the Ph.D. degree from the Key Laboratory of Advanced Transducers and Intelligent Control System of Ministry of Education, College of Physics and Optoelectronics, Taiyuan University of Technology, Taiyuan, China. His research interests include distributed optical fiber sensors and engineering applications.

Xiaohui Xue received the Ph.D. degree in geotechnical engineering from Chang'an University, Xi'an, China, in 2020. He is currently an Associate Professor with the Key Laboratory of Advanced Transducers and Intelligent Control System of Ministry of Education, Taiyuan University of Technology, Taiyuan, China. His research focuses on the application of distributed optical fiber sensor in engineering.

Mingjiang Zhang (Member, IEEE) received the Ph.D. degree in optics engineering from Tianjin University, Tianjin, China, in 2011. During 2015–2016, he was a Visiting Scholar with the University of Ottawa, Ottawa, ON, Canada. He is currently a Professor with the Taiyuan University of Technology, Taiyuan, China. He has coauthored more than 100 journal and conference papers. His research interests include the nonlinear dynamics of laser diodes, photonic-integrated broadband chaotic semiconductor laser, optical fiber sensing, and microwave photonics. Prof. Zhang is a Member of the Optical Society of America, a Senior Member of Chinese Optical Society and a Member of the Council of Chinese Instrument Society. His dissertation was selected to the National Excellent Doctoral Dissertation nomination papers of China.